crystals

MDPI

Article

Microstructure and Corrosion Resistance of Selective Laser-Melted TC4 Alloy

Shulin Gong, Yan Li *, Yanchun Li, Meihui Song, Yu Zhang, Ye Kuang and Changyao Gui

Institute of Advanced Technology, Heilongjiang Academy of Sciences, Harbin 150000, China
* Correspondence: liyan@iathas.ac.cn

Abstract

TC4 alloy samples were fabricated via selective laser melting (SLM) under different process parameters. The effects of scanning speed and build orientation on the microstructure and corrosion behavior were systematically investigated using optical microscopy (OM), scanning electron microscopy (SEM), electron backscatter diffraction (EBSD), X-ray diffraction (XRD), and electrochemical measurements. The results show that when increasing scan speed, TC4 alloy consists primarily of α/α' phases with a minor amount of β phase, along with grain refinement and a higher fraction of low-angle grain boundaries. In 3.5% NaCl solution, the XOY-oriented sample processed at 1000 mm s^{-1} exhibited higher impedance and formed a stable, highly protective passive film. In simulated body fluid, the XOY orientation at 1200 mm s^{-1} displayed a larger capacitive arc, indicating superior corrosion resistance. These findings demonstrate that the corrosion performance of SLM-processed TC4 alloy can be optimized for specific service environments by tailoring both process parameters and build orientation.

Keywords: TC4 alloy; selective laser melting; microstructure; corrosion resistance

1. Introduction

Ti-6Al-4V (TC4), a typical α + β titanium alloy, exhibits excellent mechanical properties, corrosion resistance, and favorable biocompatibility [1], making it widely used in biomedical, rail transit, and aerospace industries [2,3]. However, conventional subtractive manufacturing of TC4 alloy suffers from low material utilization and difficulty in fabricating complex geometries, which limits its broader application. The rapid development in additive manufacturing (AM), a process whereby material is deposited in layers, has effectively addressed these constraints and has seen a surge in adoption in recent years.

Selective laser melting (SLM), an additive manufacturing technique, offers reduced processing steps and shorter production cycles compared to conventional methods while enabling the fabrication of complex geometries with minimal material waste [4,5]. However, the steep thermal gradients inherent in SLM often lead to anisotropic microstructures and properties [6]. This leads to thermal stress accumulation, resulting in segregation and the formation of non-equilibrium phases [7]. Qi et al. [1] used different scanning strategies to laser-melt deposit a TC4 alloy. The results demonstrated that the morphology of the basket-like microstructure was altered by the scanning strategies employed, consequently influencing the mechanical properties of the TC4 alloy. TC4 alloy exhibited maximum tensile and yield strengths under the helical scanning strategy, whereas the unidirectional scanning strategy yielded the lowest tensile and yield strengths. Feng et al. [8] reported that post-process heat treatment of SLM-fabricated TC4 reduced tensile and yield strengths

Check for updates

Received: 6 March 2026
Revised: 3 April 2026
Accepted: 10 April 2026
Published: 9 May 2026

Copyright: © 2026 by the authors. Licensee MDPI, Basel, Switzerland. This article is an open access article distributed under the terms and conditions of the Creative Commons Attribution (CC BY) license.

but increased elongation at fracture, accompanied by a transition from ductile-brittle mixed fracture in the as-built state to fully ductile fracture. Liu et al. [9] investigated the impact of remelting parameters on the forming quality of SLM TC4 alloy. The results show that increasing remelting power and frequency, along with optimizing the scan direction, significantly improve surface quality. Higher frequency minimizes surface defects, while a reciprocating laser strategy is the most effective for achieving a superior surface finish. With regard to corrosion resistance, Li et al. [10] showed that all ultra-fine grained pure Ti processed by ECAP exhibited significantly lower corrosion current density and higher polarization resistance compared to the original coarse-grained pure Ti, demonstrating superior seawater corrosion resistance. Li et al. [11] employed both continuous-wave and pulsed laser welding to weld Ti-6Al-4V alloy and found that the pulsed mode resulted in a finer grain size. Corrosion resistance was optimal at 50 Hz, and corrosion behavior was primarily influenced by grain size and the kernel average misorientation value.

Previous studies on additive manufacturing of titanium alloys have predominantly focused on the influence of printing parameters on the mechanical properties of TC4 alloy, while its corrosion behavior in different environments remains insufficiently investigated. In SLM, using inappropriate process parameters can lead to complex heat transfer conditions that reduce the quality of the forming process and have a significant impact on the surface finish, microstructure and corrosion performance of TC4 parts. As this alloy is being used more and more in aggressive environments, including seawater and the human body, it is now an urgent research priority to understand its corrosion resistance. This study investigates the influence of SLM processing parameters on the microstructure and corrosion resistance of TC4 alloy. By optimizing the interplay between process parameters and build orientation, the corrosion performance of SLM-fabricated TC4 was enhanced under various environmental conditions. These findings provide a theoretical foundation for the fabrication of high-performance titanium alloys.

2. Experimental

2.1. Experimental Materials

Ti6Al4V alloy powder with a particle size of 15–53 μm was used as the raw material, and its morphology and elemental distribution are presented in Figure 1, and the chemical composition is shown in Table 1.

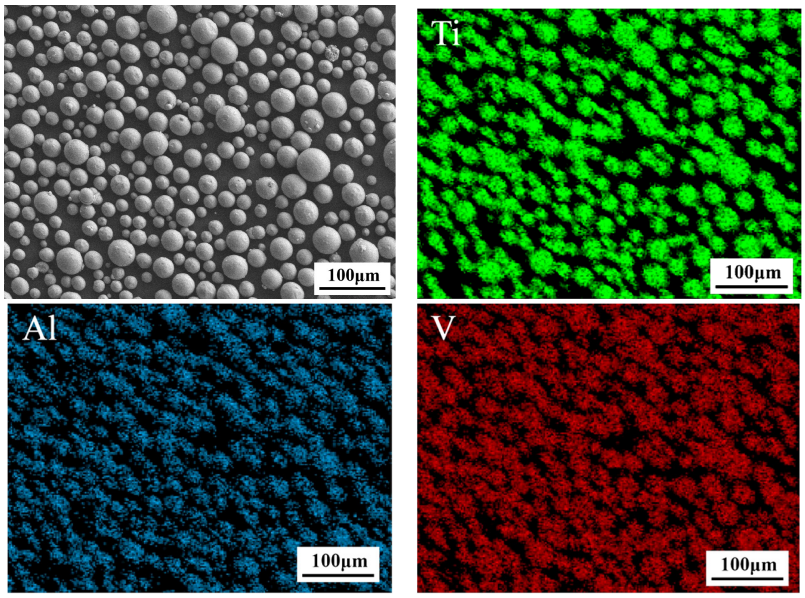

Figure 1. Morphology and elemental distribution of TC4 alloy powder.

Table 1. The chemical composition of Ti6Al4V.

Elements	Al	V	Ti
content	5.5–6.75	3.5–4.5	Bal.

The TC4 alloy was fabricated using an EOS M290-type metal 3D printer (EOS GmbH, Krailling, Germany) with the aforementioned powder, as illustrated in Figure 2. The corresponding process parameters are summarized in Table 2.

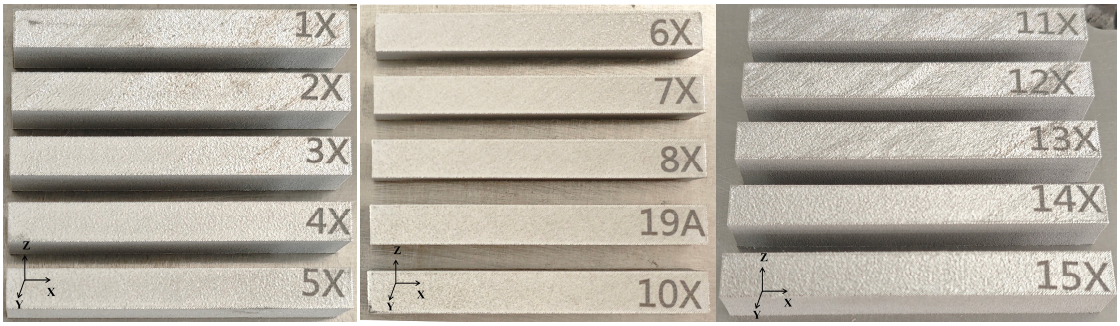

Figure 2. SLM-formed TC4 alloy.

Table 2. SLM process parameters.

Number	Laser Power W	Scanning Speed mm s^{-1}	Hatch Spacing mm	Layer Thickness mm	Energy Density J/mm^3
1–5	180	800	0.1	0.03	75
6–10	180	1000	0.1	0.03	60
11–15	180	1200	0.1	0.03	50

2.2. Testing and Characterization

The printed specimens were subjected to wire cutting to dimensions of 10 mm × 12 mm × 15 mm. Cross-sections of the cut specimens, both perpendicular to the build direction (XOY) and parallel to the build direction (XOZ), were sequentially ground using 400, 600, 800, 1000, 1200, and 2000 grit sandpaper. These were then polished and etched using Kroll's reagent. The microstructure of the TC4 alloy was examined using optical microscopy (OM), scanning electron microscopy (SEM, TESCAN AMBER, Brno, Czech Republic), and electron backscatter diffraction (EBSD, HKLNordlysS, Oxford Instruments, Abingdon, UK). The phase structure under different processes was analyzed using a DX-2700B X-ray diffractometer (Dandong Haoyuan Instrument Co., Ltd., Dandong, China) with a diffraction angle range of 20–90° and a scanning speed of 4°/min.

In order to simulate the corrosion resistance of the TC4 alloy in both seawater and human body environments, an Ivium electrochemical workstation (Ivium Technologies, Eindhoven, The Netherlands) was employed, with electrolytes comprising a 3.5% NaCl solution and simulated body fluid (SBF). The experiment employed a three-electrode system, comprising a platinum counter electrode, a saturated calomel electrode (SCE), and a working electrode. All the electrochemical measurements were repeated three times to ensure reproducibility. The corrosion tests were carried out at room temperature. The sample surface was ground with abrasive papers of 400, 600, 800, 1000, 1200, and 2000 grit, followed by polishing with 1 μm polishing paste. In order to obtain electrochemical impedance spectroscopy (EIS) and polarization curve tests, the XOY and XOZ surfaces were immersed in the electrolyte for a period of 1800 s. Following the stabilization of the open-circuit potential (OCP), the experimental setup involved the conduction of electrochemical

impedance spectroscopy (EIS) measurements across a frequency range extending from 10^{-2} Hz to 10^{5} Hz. The ensuing results underwent a process of fitting and analysis. During the course of the experiments, dynamic polarization tests were conducted at a scan rate of 1 mV/s within a potential range of −1.5 V to 1.5 V.

3. Results and Discussion

3.1. Process Parameters for Phase Structure Analysis

Figure 3 shows the XRD patterns for different orientations and scanning speeds, where Figure 3a corresponds to the XOY direction and Figure 3b to the XOZ direction. The TC4 alloy primarily consists of α/α′ phases with a small amount of β phase present. Due to the rapid cooling rate inherent in selective laser melting (SLM), most of the β phase transforms into α′ phase via shear transformation during cooling, while a small amount of α phase forms through diffusion, and a trace amount of β phase is retained. For SLM-fabricated TC4 alloy, the types of phase structures remain consistent across different scanning speeds and build orientations, although the diffraction peak heights vary. This variation likely arises from differences in the energy density input into the material at different scanning speeds, which leads to changes in the extent of α′ phase transformation [12].

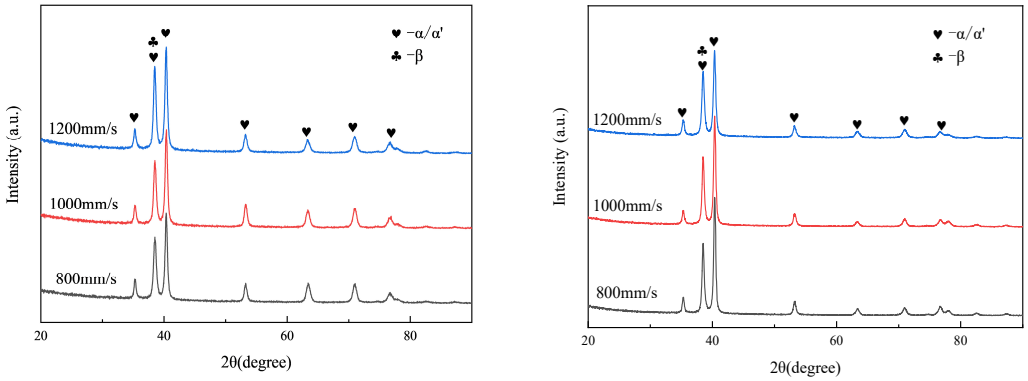

Figure 3. XRD at different scanning speeds and orientations: (**a**) XOY and (**b**) XOZ.

3.2. Effect of Process Parameters on Microstructure

This experiment investigates the effect of scanning speed on the microstructure of SLM-fabricated TC4 alloy. Scanning speed influences the energy density input by modulating the residence time of the heat source in the molten pool, thereby affecting powder melting behavior and ultimately the microstructure and properties [13]. Figure 4 shows the microstructures obtained at three scanning speeds for different build orientations. The microstructure consists mainly of fine acicular martensitic α′ structures with a basket-weave morphology, and no significant defects such as pores or cracks are detected.

Figure 5 shows the SEM microstructure of the TC4 alloy, which primarily consists of acicular features. As the scanning speed increases, these acicular structures become progressively finer. Combined with the XRD analysis, it is evident that the α/α′ phase, the dominant phase in the TC4 alloy, is uniformly distributed in a lamellar pattern within the β matrix. This morphology arises because larger β grains form in the high-temperature region. Owing to the extremely high cooling rate inherent in SLM (10^{5}–10^{8} K/s), which far exceeds the critical cooling rate for martensitic transformation, the β phase undergoes a diffusionless transformation into an α′ acicular martensitic structure [14]. Furthermore, the specific crystallographic orientation relationship between the α′ and β phases enables the α′ phase to exhibit a uniform orientation within a defined range. The retained β phase also provides nucleation sites that accelerate the nucleation rate, promoting the formation of finer acicular

structures at specific locations [15]. This microstructural evolution is attributed to the shear-induced transformation of the β phase into a supersaturated hexagonal structure under the influence of the extremely high cooling rate.

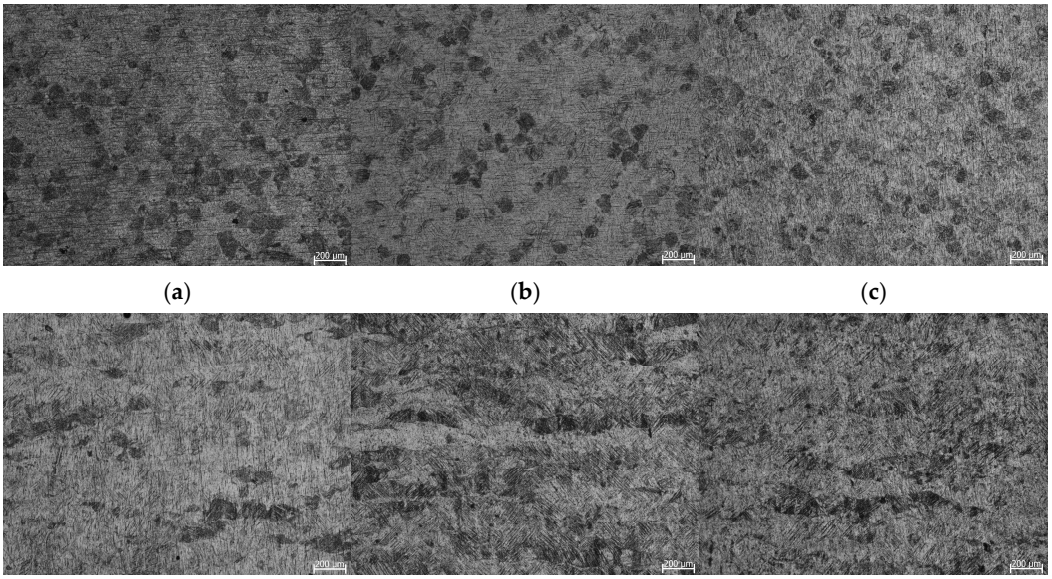

(**a**) (**b**) (**c**)

(**d**) (**e**) (**f**)

Figure 4. Microstructure under OM at different scanning speeds: (**a**) XOY 800 mm s^{-1}; (**b**) XOY 1000 mm s^{-1}; (**c**) XOY 1200 mm s^{-1}; (**d**) XOZ 800 mm s^{-1}; (**e**) XOZ 1000 mm s^{-1}; (**f**) XOZ 1200 mm s^{-1}.

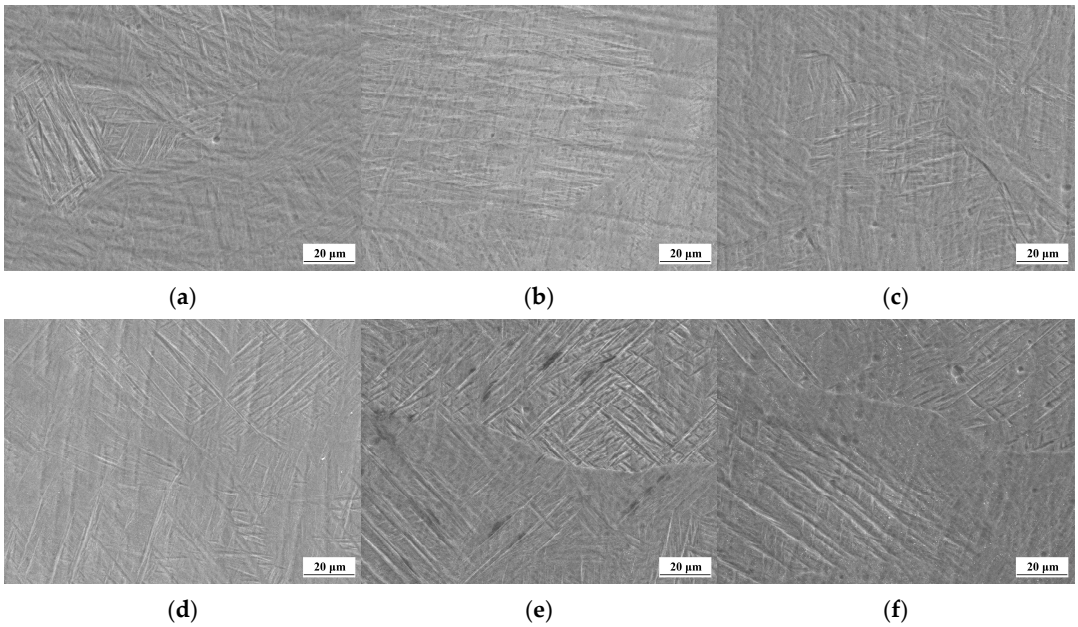

(**a**) (**b**) (**c**)

(**d**) (**e**) (**f**)

Figure 5. Microstructure under SEM at different scanning speeds: (**a**) XOY 800 mm s^{-1}; (**b**) XOY 1000 mm s^{-1}; (**c**) XOY 1200 mm s^{-1}; (**d**) XOZ 800 mm s^{-1}; (**e**) XOZ 1000 mm s^{-1}; (**f**) XOZ 1200 mm s^{-1}.

To further investigate the influence of scanning speed on the microstructural characteristics of the SLM-formed TC4 alloy, including phase distribution, grain orientation, and texture intensity, the XOY and XOZ planes were studied and analyzed at different scanning speeds. Figure 6 presents the phase distribution map obtained by EBSD, in which the red regions are predominantly occupied by the α/α' phase, while the green regions correspond to a small fraction of the β phase. As the scanning speed increases, the fraction of high-angle grain boundaries (HAGBs) on the XOY plane decreases from 94% to 92.9%, while the

fraction of low-angle grain boundaries (LAGBs) increases from 6% to 7.1%. Similarly, on the XOZ plane, the fraction of HAGBs on the XOZ plane decreases from 95.2% to 94.4%, while the fraction of LAGBs increases from 4.8% to 5.6%, in Table 3. The cooling rate of the molten pool rises, leading to greater grain refinement and a more uniform grain boundary distribution [16]. As the scanning speed increases, fine acicular α′ phases are distributed around the β phases. Meanwhile, some of these α′ phases exhibit a preferred orientation. At a scanning speed of 800 mm s^{-1}, the β phase is relatively abundant and continuously distributed; as the scanning speed increases, the β phase becomes discretely distributed in a particulate form on the surface.

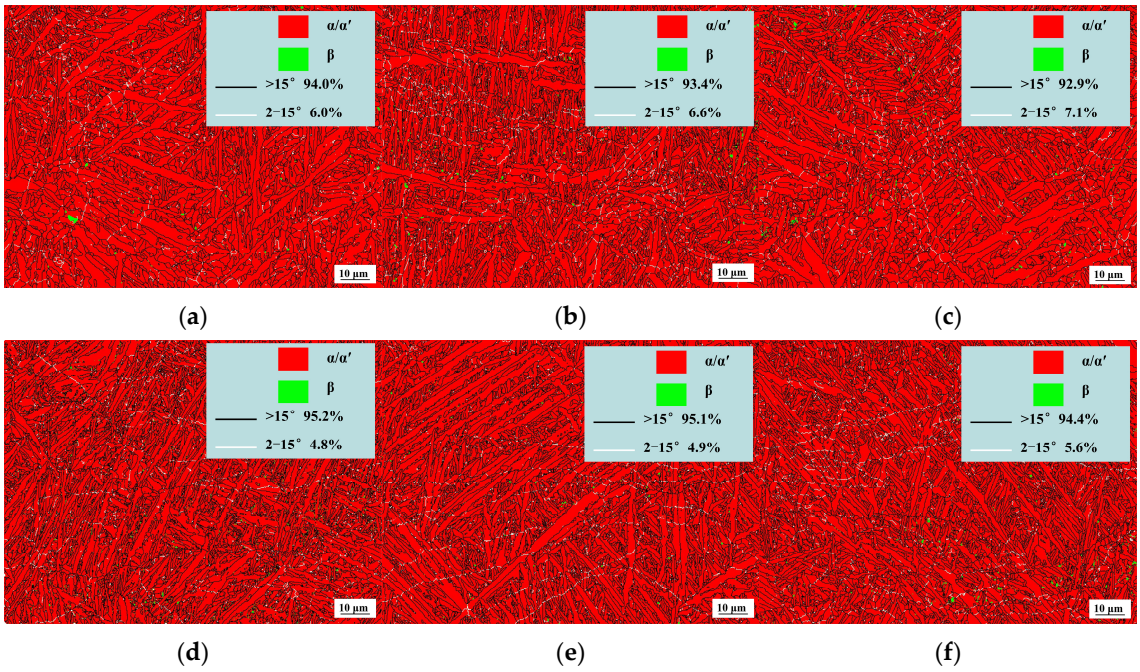

Figure 6. Phase map + grain boundaries at different scanning speeds: (**a**) XOY 800 mm s^{-1}; (**b**) XOY 1000 mm s^{-1}; (**c**) XOY 1200 mm s^{-1}; (**d**) XOZ 800 mm s^{-1}; (**e**) XOZ 1000 mm s^{-1}; (**f**) XOZ 1200 mm s^{-1}.

Table 3. High-angle grain boundaries and low-angle grain boundary fraction.

Scanning Speed mm s^{-1}	Orientation	HAGBs	LAGBs
800	XOY	94%	6.0%
	XOZ	95.2%	4.8%
1000	XOY	93.4%	6.6%
	XOZ	95.1%	4.9%
1200	XOY	92.9%	7.1%
	XOZ	94.4%	5.6%

Figure 7 presents the IPF (inverse pole figure) maps and grain size distributions of the TC4 alloy prepared at different scanning speeds. As the scanning speed increases, the grains become progressively refined. For the XOY orientation, the average grain size decreases from 4.92 μm at 800 mm s^{-1} to 4.71 μm at 1200 mm s^{-1}, while for the XOZ orientation, the average grain size decreases from 4.56 μm at 800 mm s^{-1} to 4.03 μm at 1200 mm s^{-1}. The color distribution in the IPF maps reveals the crystallographic texture: fine grains are interwoven within the columnar β grains, forming a basket-weave microstructure. At a scanning speed of 800 mm s^{-1} in the XOY orientation, most grains exhibit similar colors, indicating a concentrated crystallographic orientation along a specific direction. However,

as the scanning speed further increases, the color distribution becomes more diverse, suggesting increased grain orientation diversity. This phenomenon is attributed to the regulating effect of scanning speed on grain growth. At lower scanning speeds, the higher energy density leads to increased heat input, promoting grain growth along the maximum temperature gradient and resulting in coarser grains with a consistent orientation. As the scanning speed increases, the corresponding decrease in energy density reduces the molten pool size, and constitutional supercooling further refines the grains, increases nucleation sites, and leads to a more dispersed grain orientation.

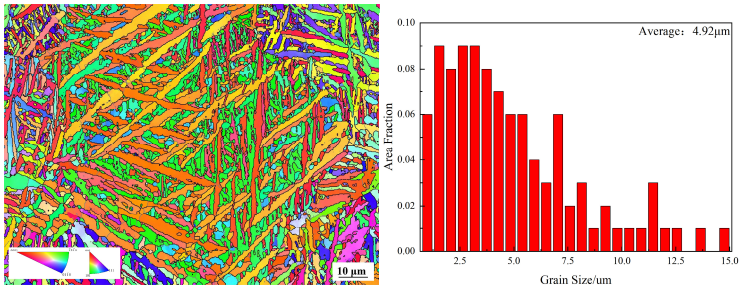

(**a**)

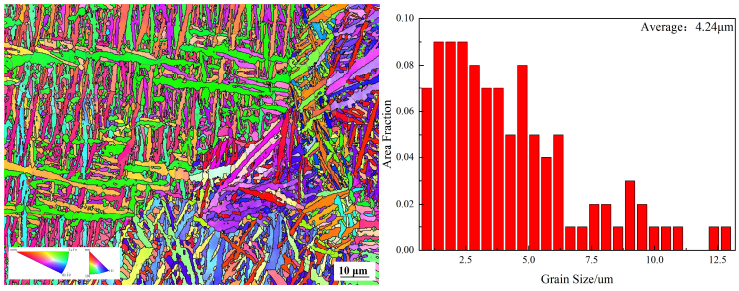

(**b**)

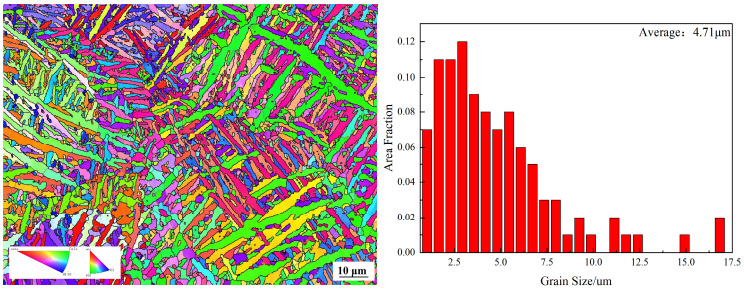

(**c**)

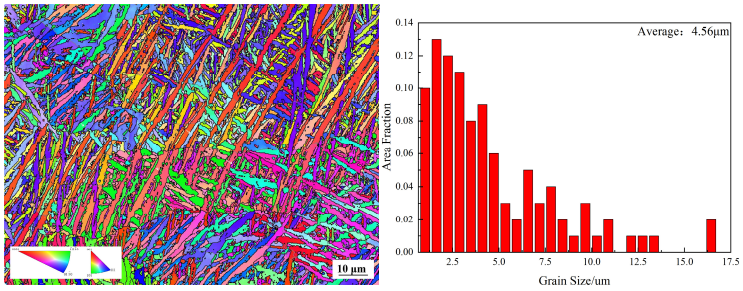

(**d**)

Figure 7. *Cont.*

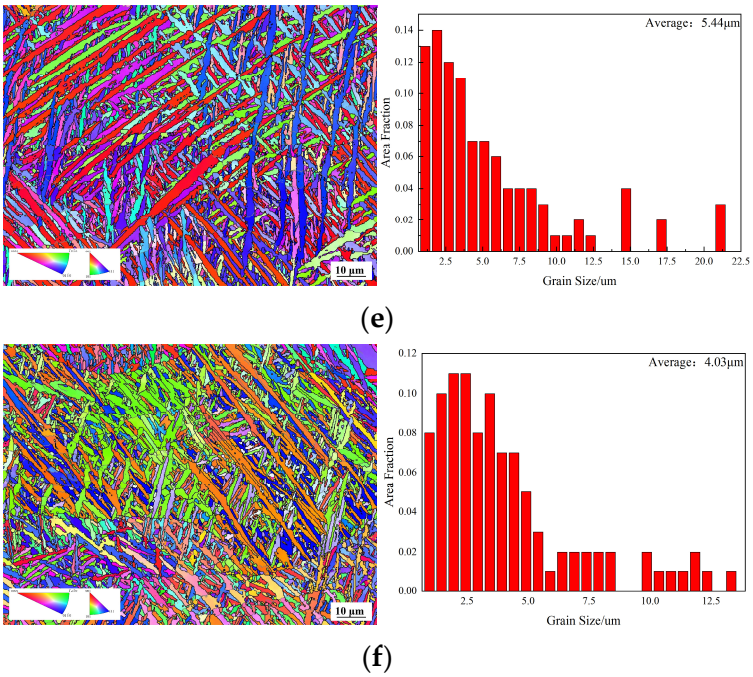

Figure 7. Inverse pole figure + grain boundaries and grain size distributions at different scanning speeds: (**a**) XOY 800 mm s^{-1}; (**b**) XOY 1000 mm s^{-1}; (**c**) XOY 1200 mm s^{-1}; (**d**) XOZ 800 mm s^{-1}; (**e**) XOZ 1000 mm s^{-1}; (**f**) XOZ 1200 mm s^{-1}.

Figures 8 and 9 show the pole figures of the α/α' phase and β phase at different scanning speeds for the XOY and XOZ orientations, respectively. For the XOY orientation, as the scanning speed increases, the maximum texture intensities of the α/α' phase are 21.93, 13.62 and 14.20, respectively, while those of the β phase are 16.87, 21.67 and 18, respectively. For the XOZ orientation, as the scanning speed increases, the maximum texture intensities of the α/α' phase are 14.36, 32.41 and 16.02, respectively, while those of the β phase are 16.17, 21.14 and 29.68, respectively. For the XOY orientation (perpendicular to the build direction), this indicates that increasing the scanning speed breaks up the growing dendrites, resulting in more random grain orientations and consequently a decrease in the texture intensity of the α/α' phase. The increased driving force for the $\beta \rightarrow \alpha/\alpha'$ phase transformation further contributes to a more dispersed orientation distribution of the α/α' phase. The slight increase in texture intensity at certain speeds may be attributed to the formation of locally aligned grain clusters under high scanning speeds, which locally enhances texture strength. For the XOZ orientation, the initial increase followed by a decrease in α/α' texture intensity can be explained by the inheritance of the parent β phase orientation at lower speeds; as scanning speed increases, the martensitic transformation becomes more random, thereby weakening the α/α' texture [17]. The gradual increase in β phase texture intensity may result from the combined effects of molten pool morphology and heat flux direction, promoting more consistent growth along the build direction.

Figures 10 and 11 show the inverse pole figures (IPFs) of the α/α' phase and β phase at different scanning speeds. This indicates that the overall intensity of the α/α' phase in the XOY plane is relatively low, suggesting a more random crystallographic distribution. Meanwhile, the β phase exhibits gradually increasing texture intensity, indicating anisotropy. For the XOZ orientation, the α/α' phase intensity first increases and then decreases with scanning speed. This trend suggests that at 1000 mm s^{-1}, the parent β phase retains a strong preferred orientation; as the scanning speed further increases, the orientation becomes progressively dispersed. Concurrently, the β phase continues to strengthen,

showing increasingly consistent crystallographic alignment, which confirms anisotropy in this direction [18].

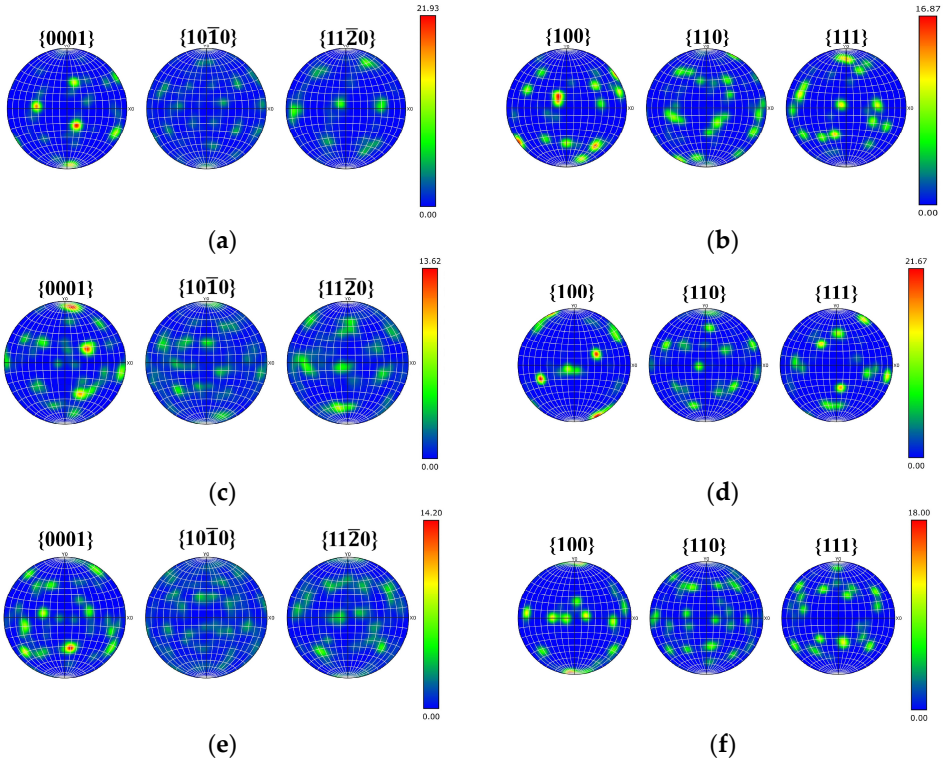

Figure 8. Pole figures in the XOY: (**a**) 800 mm s^{-1} α/α′; (**b**) 800 mm s^{-1} β; (**c**) 1000 mm s^{-1} α/α′; (**d**) 1000 mm s^{-1} β; (**e**) 1200 mm s^{-1} α/α′; (**f**) 1200 mm s^{-1} β.

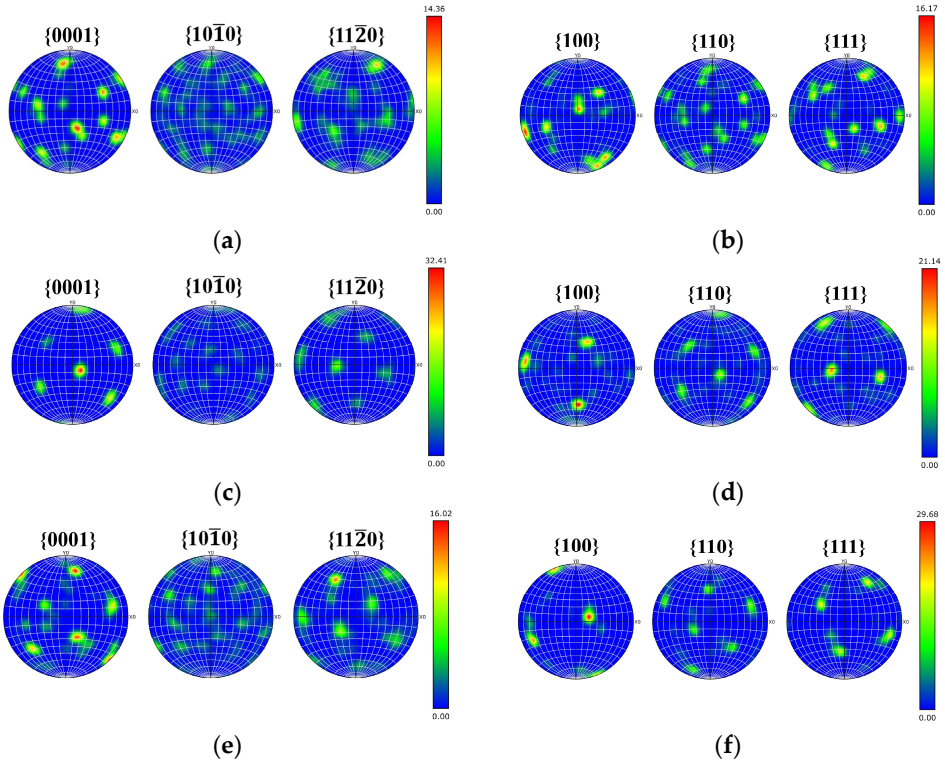

Figure 9. Pole figures in the XOZ: (**a**) 800 mm s^{-1} α/α′; (**b**) 800 mm s^{-1} β; (**c**) 1000 mm s^{-1} α/α′; (**d**) 1000 mm s^{-1} β; (**e**) 1200 mm s^{-1} α/α′; (**f**) 1200 mm s^{-1} β.

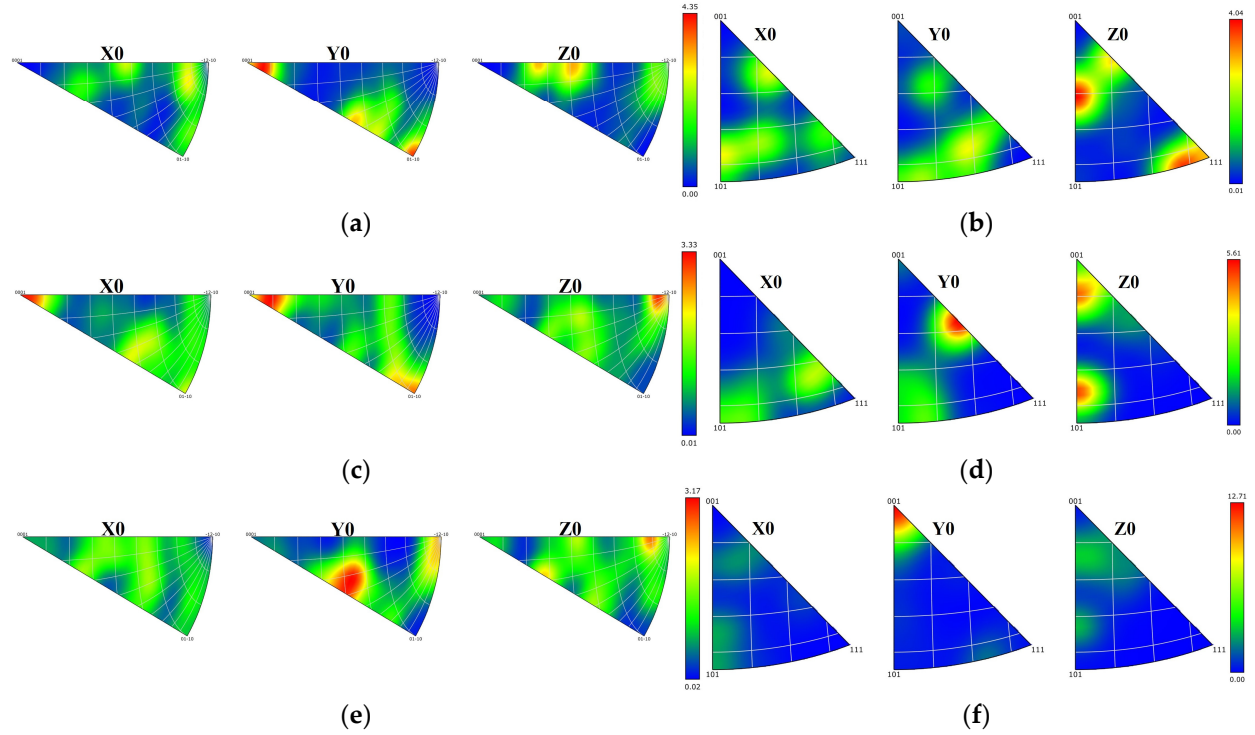

Figure 10. Inverse pole figure in the XOY: (**a**) 800 mm s^{-1} α/α'; (**b**) 800 mm s^{-1} β; (**c**) 1000 mm s^{-1} α/α'; (**d**) 1000 mm s^{-1} β; (**e**) 1200 mm s^{-1} α/α'; (**f**) 1200 mm s^{-1} β.

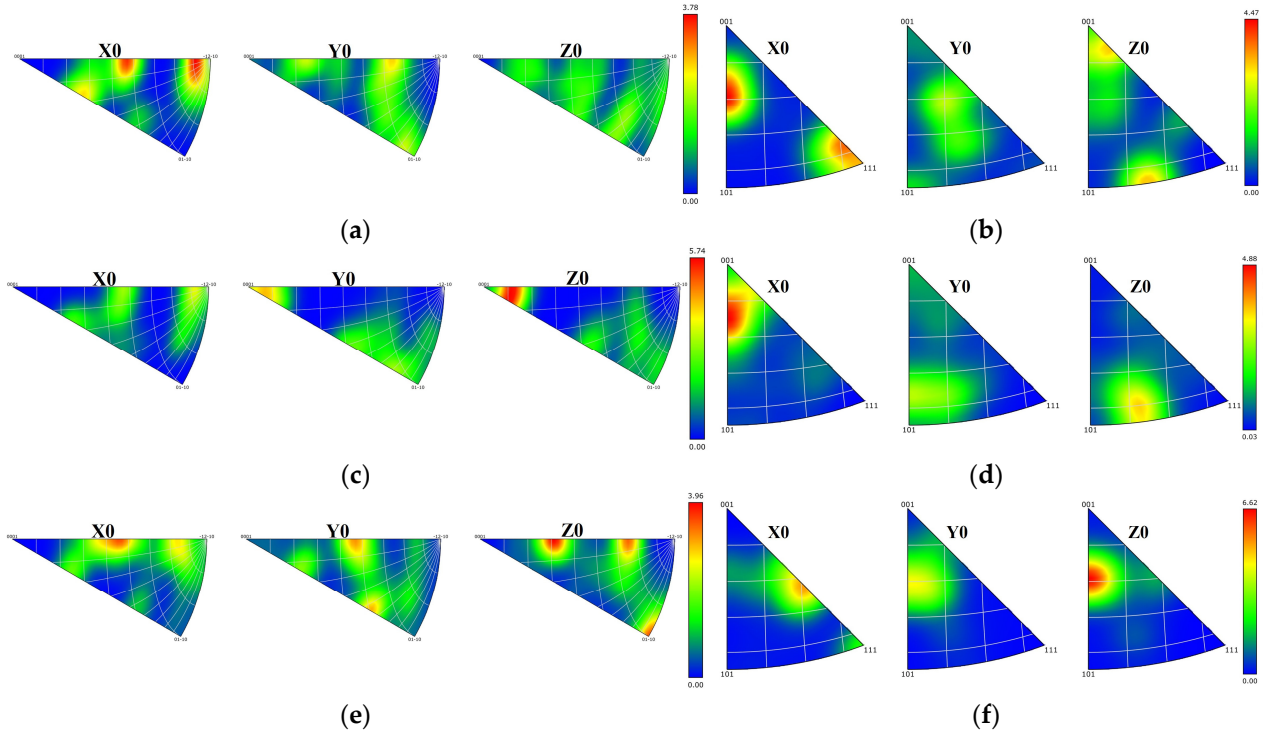

Figure 11. Inverse pole figure in the XOZ: (**a**) 800 mm s^{-1} α/α'; (**b**) 800 mm s^{-1} β; (**c**) 1000 mm s^{-1} α/α'; (**d**) 1000 mm s^{-1} β; (**e**) 1200 mm s^{-1} α/α'; (**f**) 1200 mm s^{-1} β.

Figure 12 shows the KAM (kernel average misorientation) + GB (grain boundary) maps at different orientations and scanning speeds. The KAM maps allow differentiation between the α/α' phases. The α' phase, which results from martensitic transformation, is characterized by a high density of dislocations and small orientation gradients. This gives it a green appearance on the KAM maps. In contrast, the α phase, formed through diffusion-

controlled transformation, has a low KAM value and appears as uniform blue regions. Additionally, the KAM maps reveal that white low-angle grain boundaries coincide with green regions of high KAM values, clearly indicating the presence of low-angle grain boundaries formed between different martensite variants. As the scanning speed increases, the proportion of low-angle grain boundaries gradually increases. This is attributed to the higher volume fraction of the α' martensitic phase and the finer martensite laths; as the number of variants increases, the total length and density of interfaces between variants also increase, leading to a higher proportion of low-angle grain boundaries.

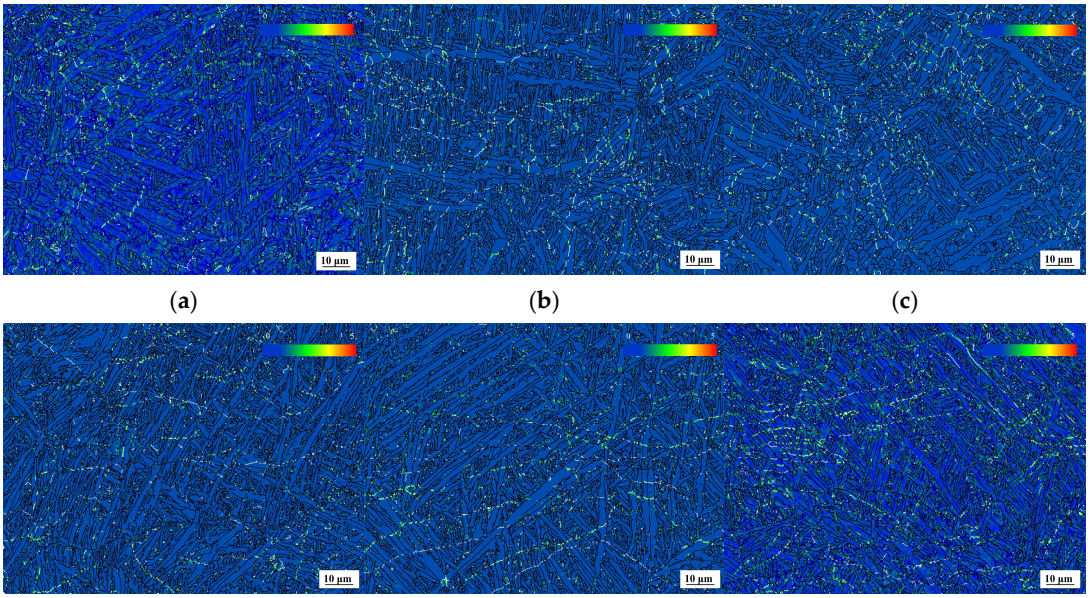

(**a**) (**b**) (**c**)

(**d**) (**e**) (**f**)

Figure 12. KAM + GB maps at different scanning speeds: (**a**) XOY 800 mm s^{-1}; (**b**) XOY 1000 mm s^{-1}; (**c**) XOY 1200 mm s^{-1}; (**d**) XOZ 800 mm s^{-1}; (**e**) XOZ 1000 mm s^{-1}; (**f**) XOZ 1200 mm s^{-1}.

3.3. Analysis of Process Parameters on Corrosion Resistance

3.3.1. Corrosion Resistance Analysis in a 3.5% NaCl Solution

Electrochemical impedance was employed to investigate the kinetic processes of corrosion reactions in the TC4 alloy within a 3.5% NaCl solution under varying scan rates in different orientations, characterizing the stability and integrity of the passivation film. Figure 13a,c present the Nyquist plots for the XOY and XOZ orientations, respectively. It is evident that as the scan rate increases, the impedance spectra exhibit similar trends, both displaying a single capacitive arc. The capacitive arc exhibits a trend of first increasing and then decreasing, reaching its largest size at 1000 mm s^{-1}. The radius of the capacitive arc depends on the resistance during the electrochemical reaction process. A larger capacitive arc radius indicates greater reaction resistance, more difficult charge transfer, lower current density, and superior corrosion resistance [19]. Figure 13b,d show the Bode plots for the XOY and XOZ orientations, respectively. For the XOY orientation, the phase angle gradually increases at 800 mm s^{-1} in the mid-frequency range (10–10^2 Hz), indicating that as corrosion progresses on the metal surface, the passivation film becomes progressively uniform and dense. At 1000 mm s^{-1}, the phase angle remains relatively stable, indicating a dense and relatively uniform passivation film at this point. As the scanning speed increases, the phase angle shows a gradual decreasing trend, suggesting passivation film instability and potential breakdown [20,21]. For the XOZ direction parallel to the build axis, the overall trend is similar, indicating a well-formed passivation film at 1000 mm s^{-1}.

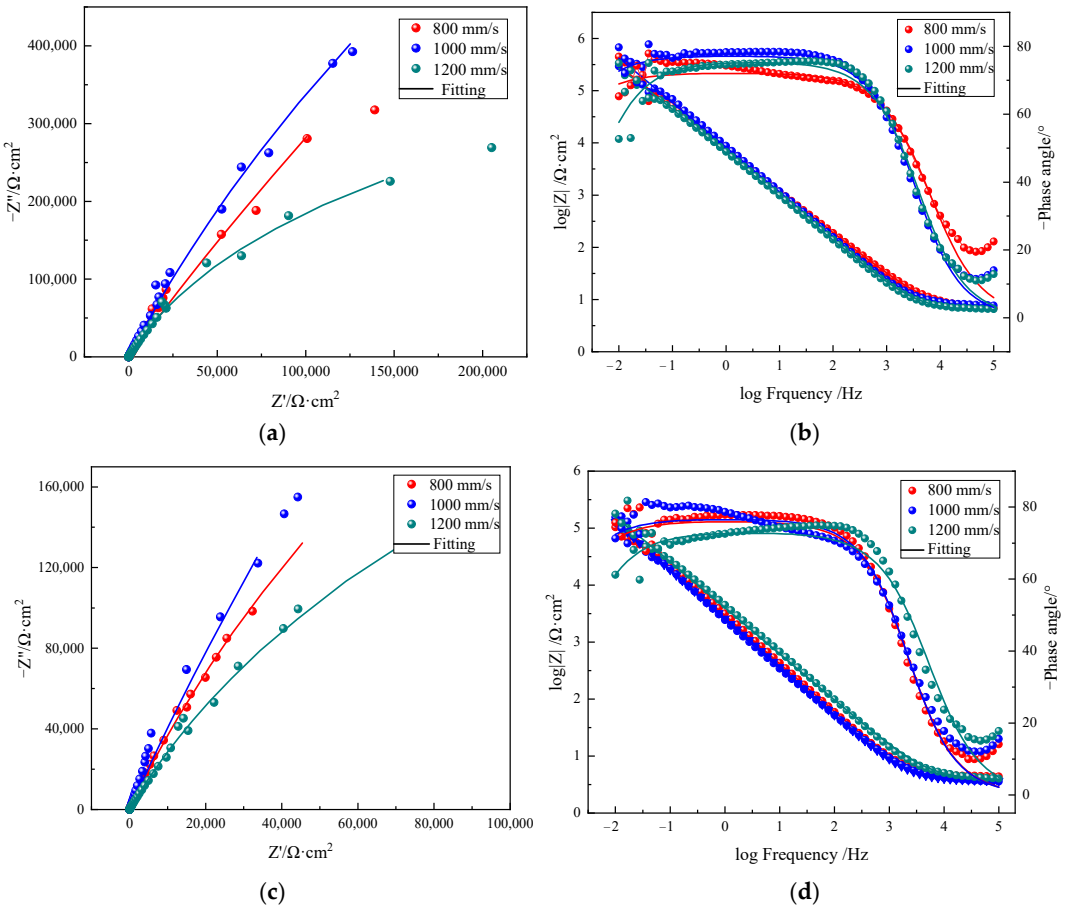

Figure 13. Nyquist and Bode plots at different scanning speeds in the 3.5% NaCl: (**a**) XOY Nyquist; (**b**) XOY Bode; (**c**) XOZ Nyquist; (**d**) XOZ Bode.

Figure 14 shows the polarization curves of the TC4 alloy in a 3.5% NaCl electrolyte at different scanning speeds and orientations. Using Tafel extrapolation, the corrosion current density (I_{corr}) of the TC4 alloy in the 3.5% NaCl electrolyte at different scanning speeds and orientations is presented in Figure 14c. For the XOY orientation, at a scanning speed of 800 mm s^{-1}, the corrosion current density was 9.37 ± 1.64 × 10^{-8} A/cm^2. As the scanning speed increased to 1200 mm s^{-1}, the corrosion current density was 6.71 ± 1.33 × 10^{-8} A/cm^2. The corrosion potential gradually decreased with increasing scanning speed, indicating that higher scanning speeds enhance the alloy's resistance to uniform corrosion and reduce its susceptibility to corrosion. For the XOZ orientation, as the scanning speed increased, the corrosion current densities were 9.21 ± 1.52 × 10^{-8} A/cm^2, 9.44 ± 1.55 × 10^{-8} A/cm^2 and 6.20 ± 1.57 × 10^{-8} A/cm^2, respectively. The corrosion current density at 1000 mm s^{-1} showed a slight increase. Combined with the phase angle in the Bode plot, the mid-frequency range exhibited a gradual increase, indicating that the passivation film formed progressively and uniformly. At this stage, weak points in the passivation film may emerge, leading to a slight rise in the corrosion current density.

As illustrated in Figure 15, the equivalent circuit of the TC4 alloy in a 3.5% NaCl solution is presented, with the fitting results documented in Table 4. R_s is defined as the solution resistance between the reference electrode and the specimen surface, while R_{ct} represents the charge transfer resistance. It is evident that Q and n are two parameters of the constant phase angle element. The quantity Q is defined as the constant phase angle element (CPE), and the constant n is understood to be the *CPE* constant, with the condition that $-1 < n < 1$. It has been demonstrated that an elevated value of n is indicative of a more substantial passivation film on the specimen surface. This film functions to more

effectively impede the corrosive medium and consequently reduce the corrosion rate of the specimen. At 1000 mm s^{-1}, R_{ct} reaches its maximum value, indicating the densest and most uniform passivation film. At a scanning speed of 800 mm s^{-1}, the passivation film exhibits the second highest density, while at 1200 mm s^{-1}, it demonstrates the lowest density. It is evident that an elevated R_{ct} value is indicative of a diminished corrosion rate of the material, thereby resulting in an enhanced level of corrosion resistance [22].

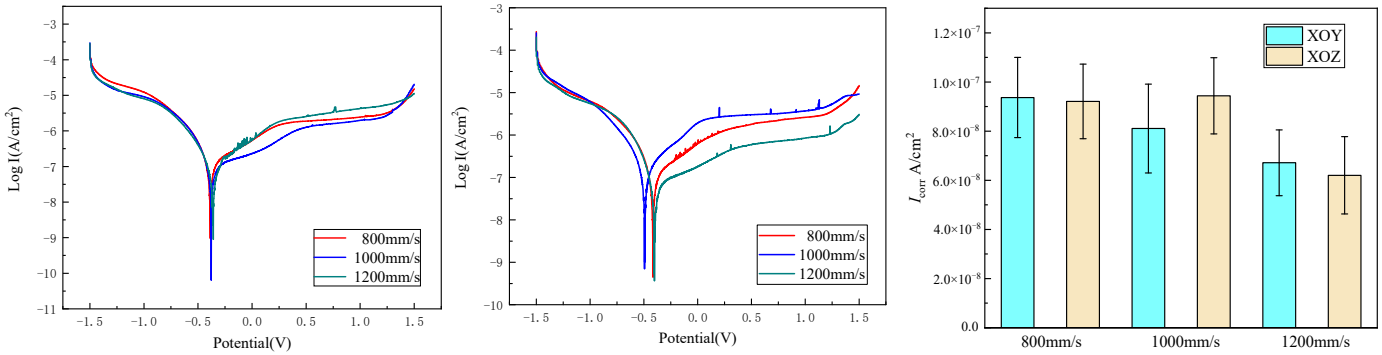

Figure 14. Polarization curves at different scanning speeds in 3.5% NaCl and statistical analysis: (**a**) XOY; (**b**) XOZ; (**c**) statistical analysis of I_{corr}.

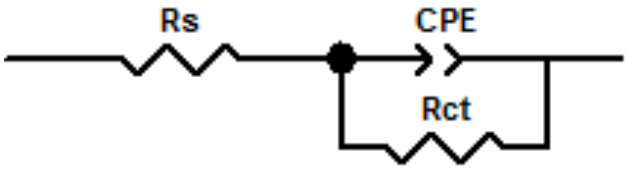

Figure 15. Schematic diagram of equivalent circuit in the 3.5% NaCl.

Table 4. Fitting parameters of equivalent analog circuit in the 3.5% NaCl.

Scanning Speed mm s^{-1}	Orientation	R_s $\Omega \cdot cm^{-2}$	R_{ct} $\Omega \cdot cm^{-2}$	n	Q $\Omega^{-1} \cdot s^n \cdot cm^{-2}$
800	XOY	7.893	6.092×10^6	0.801	2.513×10^{-5}
	XOZ	7.722	2.77×10^6	0.846	4.018×10^{-5}
1000	XOY	9.206	6.314×10^6	0.858	2.079×10^{-5}
	XOZ	6.569	3.588×10^6	0.852	4.483×10^{-5}
1200	XOY	7.562	1.014×10^6	0.838	2.758×10^{-5}
	XOZ	6.825	1.293×10^6	0.811	3.142×10^{-5}

Figure 16 shows the corrosion morphology at different scanning speeds. Overall, as the scanning speed increases, the corrosion morphology becomes relatively uniform. At 1200 mm s^{-1}, unevenly distributed pitting corrosion pits appear in the morphology, while no obvious defects such as corrosion cracks were observed in the other morphologies. Pitting corrosion may result from Cl^{2-} adsorption at defects in the passivation film, locally destabilizing the film and forming microscopic corrosion pits that subsequently trigger rapid dissolution of the substrate.

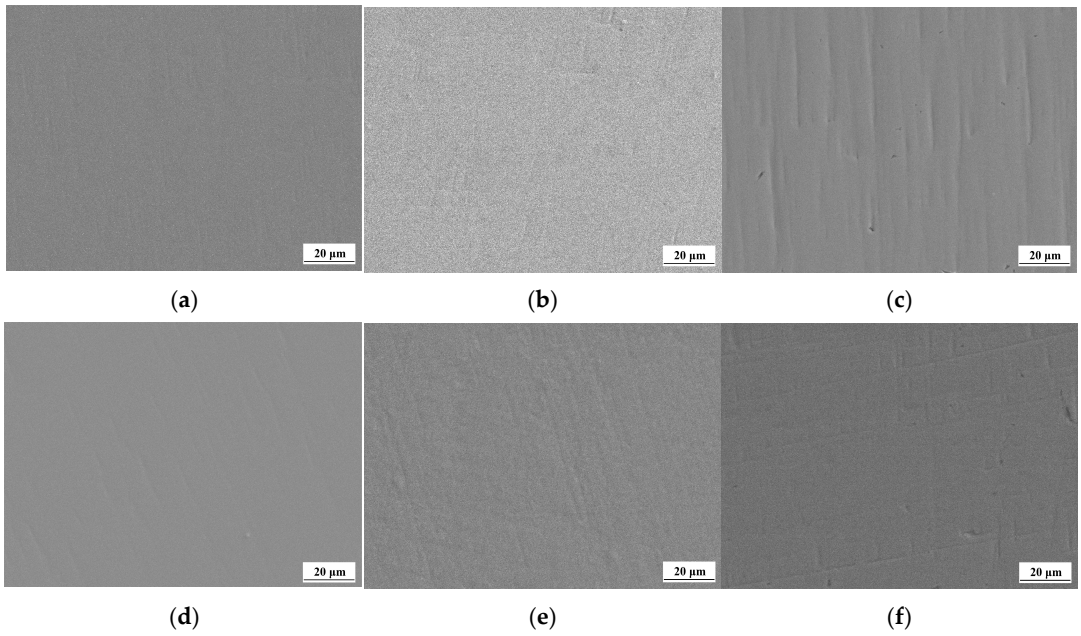

Figure 16. Corrosion morphology at different scanning speeds in the 3.5% NaCl: (**a**) XOY 800 mm s^{-1}; (**b**) XOY 1000 mm s^{-1}; (**c**) XOY 1200 mm s^{-1}; (**d**) XOZ 800 mm s^{-1}; (**e**) XOZ 1000 mm s^{-1}; (**f**) XOZ 1200 mm s^{-1}.

3.3.2. Corrosion Resistance Analysis in an SBF Solution

Figure 17a,c present the Nyquist plots for the XOY and XOZ orientations, respectively. As the scanning speed increases, the impedance spectra exhibit similar trends: the capacitive arc first decreases and then increases, reaching a larger size at 1200 mm s^{-1}. Combined with the KAM images, it is evident that increasing the scanning speed raises the proportion of low-angle grain boundaries. In the simulated body fluid (SBF), a gradual improvement in corrosion resistance is observed. As shown in Table 3, the proportion of low-angle grain boundaries (LAGBs) increases gradually with increasing scanning speed, and this increase correlates positively with the enhanced corrosion resistance observed in SBF. This correlation is consistent with previous reports on the corrosion behavior of titanium alloys in SBF environments. According to the study by Madapana et al. [23], after laser surface structuring, a large number of low-angle grain boundaries (LAGBs) are formed in the surface layer of the sample, with their area fraction significantly higher than that of the as-received annealed sample. Although these low-angle grain boundaries and their interiors exhibit high local strain, the EIS results show that the laser-structured samples have better charge transfer resistance and passive film stability than the as-received sample. As shown in Figure 17b, the phase angles exhibit minimal difference at 800 mm s^{-1} and 1000 mm s^{-1} in the XOY orientation, indicating that the passivation film formed is relatively uniform and stable. In contrast, Figure 17d reveals two phase angle peaks in the XOZ orientation, suggesting the presence of two time constants in the impedance spectrum. In the high-frequency region, the capacitive arc is associated with the corrosion product film resistance in parallel with the double-layer capacitance, while the low-frequency region corresponds to the charge transfer resistance in parallel with the double-layer capacitance. Although the Nyquist plot displays a single pronounced capacitive arc, this is likely because the two time constants are relatively close and overlap in the spectrum, resulting in an enlarged capacitive arc.

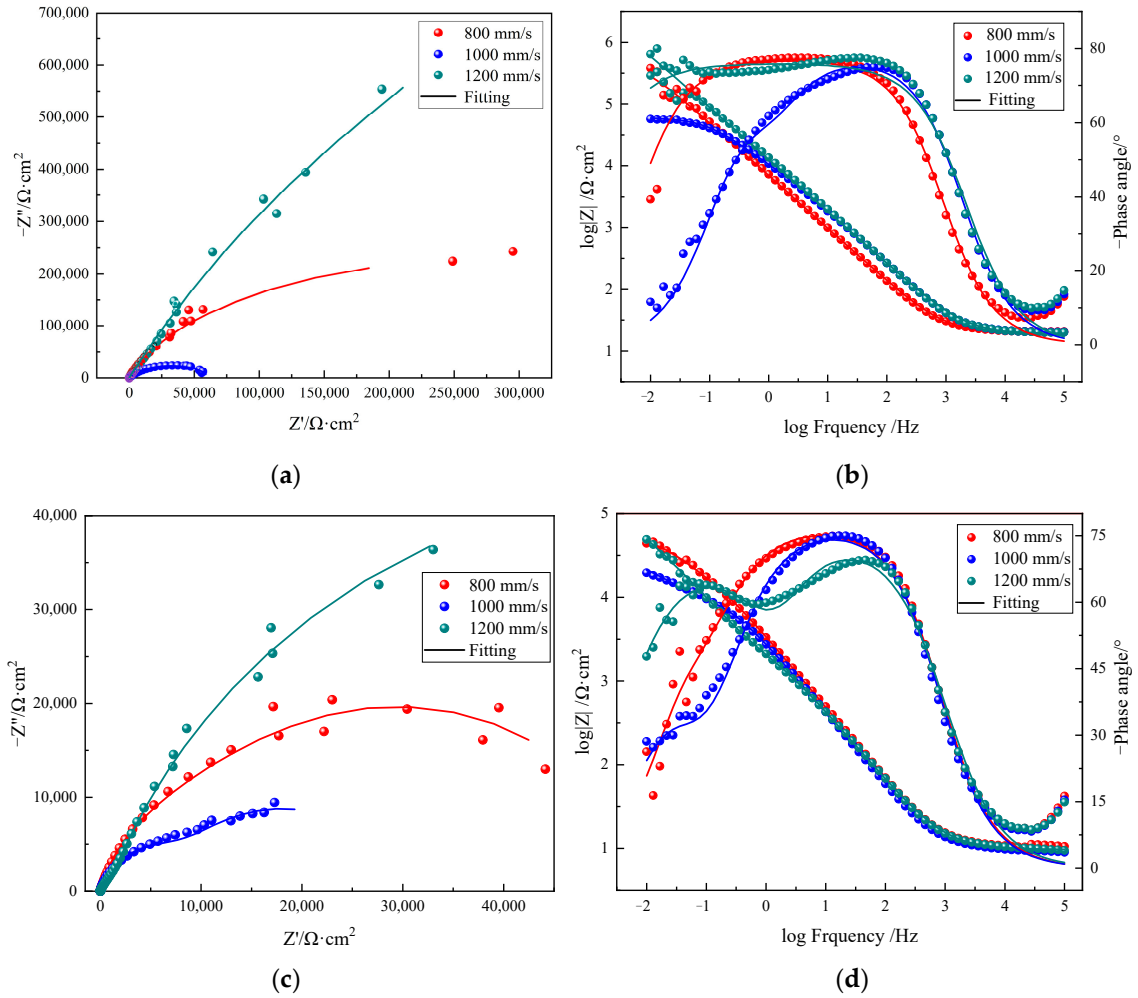

Figure 17. Nyquist and Bode plots at different scanning speeds in an SBF solution: (**a**) XOY Nyquist; (**b**) XOY Bode; (**c**) XOZ Nyquist; (**d**) XOZ Bode.

Figure 18 shows the dynamic potential polarization curves in simulated body fluid at different scanning speeds and orientations. In the XOY orientation, the corrosion current density gradually decreases with increasing scanning speed. When the scanning speed reaches 1200 mm s^{-1}, the corrosion current density can be as low as $3.03 \pm 1.77 \times 10^{-7}$ A/cm^2. Combined with the impedance plots, it is evident that in the simulated body fluid environment, increasing the scanning speed enhances the stability of the passivation film, blocks ion intrusion, and effectively suppresses the dissolution of the passivation film [24,25]. For the XOZ orientation, as the self-corrosion potential shifts positively, the current density decreases rapidly. At this stage, the substrate surface is in an activated state without a stable passivation film. As the potential continues to increase, the current density rapidly decreases upon reaching a critical value, at which point a passivation film begins to form on the surface. The substrate surface becomes covered by a dense passivation film. As the potential further increases, the current density rises sharply, causing the passivation film to break down. This ultimately leads to a current plateau, which may indicate that a stable passivation region has been reached. The corrosion reaction current density exhibits a pattern similar to that of the XOY orientation. When the scanning speed reaches 1200 mm s^{-1}, the corrosion current density can be as low as $1.76 \pm 0.77 \times 10^{-8}$ A/cm^2.

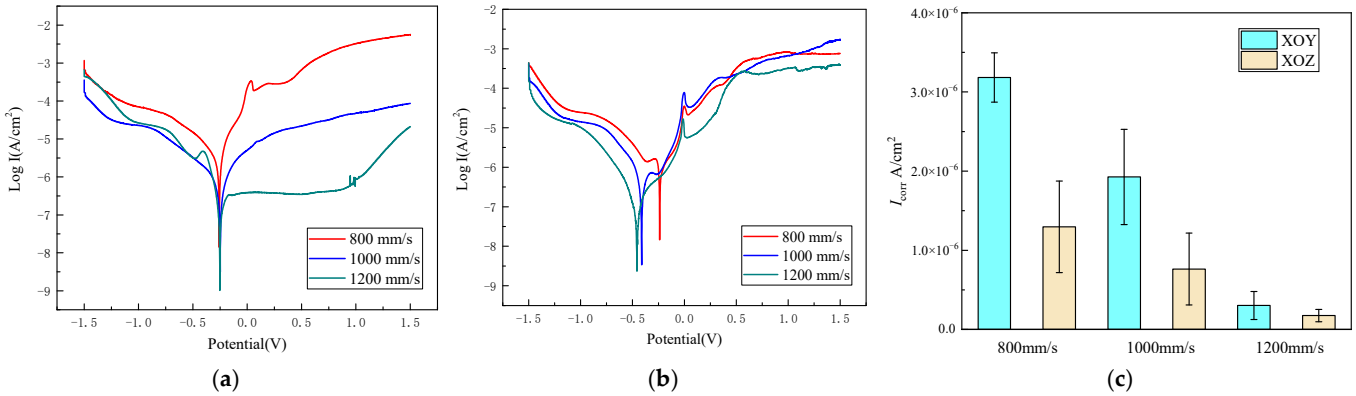

Figure 18. Polarization curves at different scanning speeds in an SBF solution: (**a**) XOY; (**b**) XOZ; (**c**) statistical analysis of I_{corr}.

Figure 19 shows the equivalent circuits of the TC4 alloy in the simulated body fluid, with the fitting results presented in Table 5. For the XOY orientation, the equivalent circuit in Figure 19a applies, while the XOZ orientation corresponds to the circuit in Figure 19b. Here, R_f represents the corrosion product film resistance, with its corresponding double-layer capacitance denoted as CPE_f. Q_f and n_f are the two parameters associated with CPE_f, where n_f gradually decreases with increasing scanning speed. This decrease may result from uneven accumulation of corrosion products, as the film layer tends to be looser at lower scanning speeds, leading to reduced n_f values.

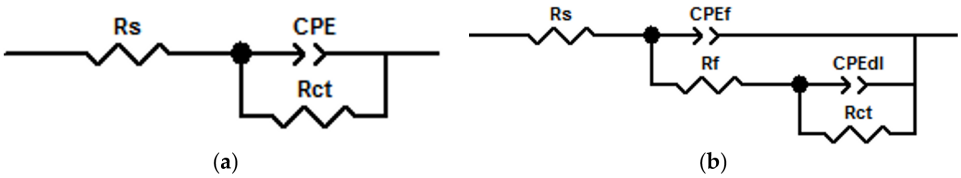

Figure 19. Schematic diagram of equivalent circuit in an SBF solution. (**a**) XOY; (**b**) XOZ.

Table 5. Fitting parameters of equivalent analog circuit in an SBF solution.

Scanning Speed mm s^{-1}	Orientation	R_s $\Omega \cdot cm^{-2}$	R_f $\Omega \cdot cm^{-2}$	n_f	Q_f $\Omega^{-1} \cdot s^n \cdot cm^{-2}$	R_{ct} $\Omega \cdot cm^{-2}$	n_{ct}	Q_{ct} $\Omega^{-1} \cdot s^n \cdot cm^{-2}$
800	XOY	24.33	-	-	-	6.935×10^5	0.858	2.467×10^{-5}
	XOZ	18.85	3.504×10^4	0.862	3.183×10^{-5}	5.947×10^4	0.730	3.160×10^{-5}
1000	XOY	22.9	-	-	-	7.123×10^4	0.834	1.553×10^{-5}
	XOZ	16.72	2.127×10^4	0.855	3.886×10^{-5}	3.784×10^4	0.786	2.577×10^{-5}
1200	XOY	22.87	-	-	-	5.938×10^6	0.845	1.396×10^{-5}
	XOZ	17.60	5.557×10^3	0.837	3.845×10^{-5}	2.317×10^5	0.750	4.586×10^{-5}

Figure 20 shows the corrosion morphology at different scanning speeds. Overall, as the scanning speed increases, the corrosion morphology becomes relatively uniform. No significant pitting corrosion was observed in the morphology at 1200 mm s^{-1}, indicating that the high impedance and low corrosion current density confer excellent corrosion resistance.

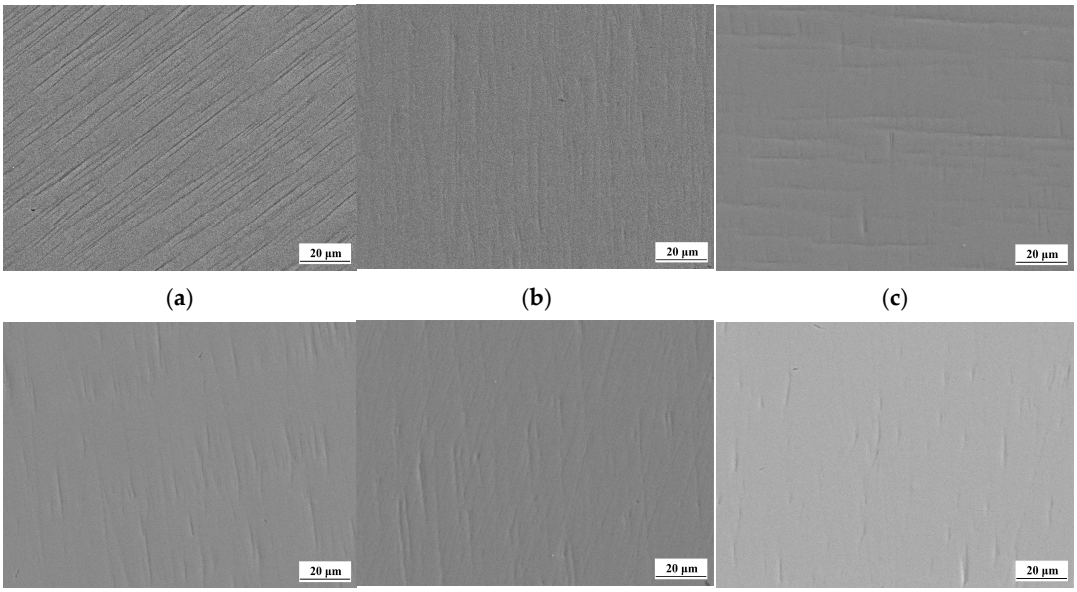

Figure 20. Corrosion morphology at different scanning speeds: in an SBF solution (**a**) XOY 800 mm s^{-1}; (**b**) XOY 1000 mm s^{-1}; (**c**) XOY 1200 mm s^{-1}; (**d**) XOZ 800 mm s^{-1}; (**e**) XOZ 1000 mm s^{-1}; (**f**) XOZ 1200 mm s^{-1}.

4. Conclusions

This study investigated the effect of scanning speed on the microstructure and corrosion behavior of selective laser-melted (SLM) TC4 alloy in 3.5 wt% NaCl solution and simulated body fluid (SBF). The main conclusions are as follows:

(1) In the SLM process for TC4 alloy, increasing the scanning speed refines the grain size and increases the proportion of low-angle grain boundaries (LAGBs) without altering the phase composition ($\alpha/\alpha' + \beta$).

(2) In 3.5% NaCl solution, higher scanning speeds reduce the rate of uniform corrosion but decrease the stability of the passive film against localized corrosion. In simulated body fluid (SBF), higher scanning speeds improve resistance to both uniform and localized corrosion. Therefore, in simulated body fluid environments, a scanning speed of 1200 mm/s offers better corrosion resistance, whereas in chloride-rich environments, 1000 mm/s provides a better balance.

Author Contributions: Conceptualization, Y.L. (Yan Li); methodology, Y.L. (Yan Li), Y.L. (Yanchun Li), Y.K. and C.G.; software, S.G. and C.G.; validation, Y.L. (Yanchun Li); formal analysis, Y.L. (Yanchun Li); investigation, Y.L. (Yan Li) and Y.Z.; resources, Y.Z.; data curation, S.G. and Y.K.; writing—original draft, S.G.; visualization, M.S.; project administration, M.S.; funding acquisition, Y.Z. All authors have read and agreed to the published version of the manuscript.

Funding: This research was funded by the Heilongjiang Academy of Sciences Institute Capacity Enhancement Special Fund grant number YSTS2025GJS01, and the Project of Scientific Research Operating Expenses for Provincial Research Institutes in Heilongjiang Province, grant number CZBZ202608001. And The APC was funded by YSTS2025GJS01.

Data Availability Statement: The data presented in this study are available on request from the corresponding author. The data are not publicly available due to privacy.

Conflicts of Interest: The authors declare that they have no known competing financial interests or personal relationships that could have appeared to influence the work reported in this paper.

References

1. Shan, Q.B.; Liu, C.; Yao, J.; Zhan, Y.; Liu, C.S. Effects of Scanning Strategy on the Microstructure, Properties, and Residual Stress of TC4 Titanium Alloy Prepared by Laser Melting Deposition. *Laser Optoelectron. Prog.* **2021**, *58*, 256–264.
2. Liu, S.F.; Song, X.; Xue, T.; Ma, N.; Wang, Y.; Wang, L.Q. Application and development of titanium alloy and titanium matrix composites in aerospace field. *J. Aeronaut. Mater.* **2020**, *40*, 77–94.
3. Jin, X.Y.; Lan, L.; Gao, S.; He, B.; Rong, Y.H. Effects of laser shock peening on microstructure and fatigue behavior of Ti-6Al-4V alloy fabricated via electron beam melting. *Mater. Sci. Eng. A* **2020**, *780*, 139199. [CrossRef]
4. Wang, W.; Zhang, L.; Dong, X.; Wu, J.; Zhou, Q.; Li, S.; Shen, C.; Liu, W.; Wang, G.; He, R. Additive manufacturing of fiber reinforced ceramic matrix composites: Advances, challenges, and prospects. *Ceram. Int.* **2022**, *48*, 19542–19556. [CrossRef]
5. Mohamad, A.; Guilé, N.M.; Bahaa, S.; Luqman, H.; Adel, J.; Ramez, A.; Peter, P. Advancements in Laser Wire-Feed Metal Additive Manufacturing: A Brief Review. *Materials* **2023**, *16*, 2030. [CrossRef] [PubMed]
6. Kok, Y.; Tan, X.P.; Wang, P.; Nail, M.L.S.; Loh, N.H.; Liu, E.; Tor, S.B. Anisotropy and heterogeneity of microstructure and mechanical properties in metal additive manufacturing: A critical review. *Mater. Des.* **2018**, *139*, 565–586. [CrossRef]
7. Tsai, M.T.; Chen, Y.W.; Chao, C.Y.; Jang, J.S.C.; Tsai, C.C.; Su, Y.L.; Kuo, C.N. Heat-treatment effects on mechanical properties and microstructure evolution of Ti-6Al-4V alloy fabricated by laser powder bed fusion. *J. Alloys Compd.* **2020**, *816*, 152615. [CrossRef]
8. Feng, E.; Chen, R.; Di, S.; Zhou, Z.; Yin, X.; Kang, N.; Lin, X. Effect of Heat Treatment on Microstructure and Mechanical Properties of TC4 Alloy by Selective Laser Melting. *Chin. J. Lasers* **2024**, *51*, 298–309.
9. Liu, Y.; Jia, S.; Shi, W.; Han, J.; Chen, X.; Zhang, X. Effect of Laser Remelting on Single Pass Quality of TC4 Selective Laser Melting. *Appl. Laser* **2024**, *44*, 10–19.
10. Li, X.; Dong, Y.; Dan, Z.; Cheng, H.; Feng, Z.; Guo, Y. Corrosion Behavior of Ultrafine Grained Pure Ti Processed by Equal Channel Angular Pressing. *Acta Metall. Sin.* **2019**, *55*, 967–975.
11. Li, Z.; Zhao, W.; Zhang, H.; Xiao, G.; Yu, K. Microstructure and corrosion resistance of fusion zone in Ti-6Al-4V alloy welded using pulsed- and continuous-wave lasers. *Corros. Sci.* **2023**, *220*, 111269. [CrossRef]
12. Zhang, J.J. Microstructure Evolution and Mechanical Properties of TC4 Alloy by Laser Direct Energy Deposition. Master's Thesis, Yanshan University, Qinhuangdao, China, 2024.
13. Tong, X.; Xu, W.; Wang, X.; Wang, Y.; Duan, J. Summary on Effect of Welding Techniques on Microstructure and Mechanical Properties of TC4 Ti-alloy Weld Joints. *J. Chin. Soc. Corros. Prot.* **2025**, *45*, 1161–1174.
14. Yu, Z.; Chen, Z.; Qu, D.; Qu, S.; Wang, H.; Zhao, F.; Zhang, C.; Feng, A.; Chen, D. Microstructure and Electrochemical Behavior of a 3D-Printed Ti-6Al-4V Alloy. *Materials* **2022**, *15*, 4473. [CrossRef]
15. Ren, Y.M.; Lin, X.; Yang, H.O.; Tan, H.; Chen, J.; Jian, Z.Y.; Li, J.Q.; Huang, W.D. Microstructural features of Ti-6Al-4V manufactured via high power laser directed energy deposition under low-cycle fatigue. *J. Mater. Sci. Technol.* **2021**, *83*, 18–33. [CrossRef]
16. Wu, H.; Luo, Z.; Jin, S. Effects of Laser Power and Laser Scanning Speed on Microstructure and Property of TC4 Titanium Alloy Formed by Selective Laser Melting. *Mater. Mech. Eng.* **2021**, *45*, 51–57.
17. Zhang, Y.; Xin, R.; Huang, X.; Liu, Q. Study on variant selection mechanism of α precipitates formed at triple junctions in metastable β titanium alloys. *J. Chin. Electron Microsc. Soc.* **2025**, *44*, 271–278.
18. Jia, Y.; Ma, Y.; Shi, R.; Zhou, Y.; Wang, Q.; Huang, S.; Qi, M.; Wang, D.; Lei, J.; Yang, R. Probing nanoscale variant distribution in a heterogenous α/β titanium alloy. *Acta Mater.* **2025**, *296*, 121148. [CrossRef]
19. Dai, N.; Zhang, L.; Zhang, J.; Zhang, X.; Ni, Q.; Chen, Y.; Wu, M.; Yang, C. Distinction in corrosion resistance of selective laser melted Ti-6Al-4V alloy on different planes. *Corros. Sci.* **2016**, *111*, 703–710. [CrossRef]
20. Liao, X.; Zheng, Z.; Liu, T.; Long, J.; Wang, S.; Zhang, H.; Zheng, K. Achieving high impact-abrasion-corrosion resistance of high-chromium wear-resistant steel via vanadium additions. *J. Mater. Res. Technol.* **2024**, *29*, 2425–2436. [CrossRef]
21. Cao, S.; Zhu, M.; Yuan, Y.; Guo, S.; Zhu, G. Corrosion Behavior of CoCrFeMnNi High Entropy Alloy in 3.5%NaCl Solution with and without 0.05 M $NaHSO_3$. *J. Mater. Eng. Perform.* **2022**, *32*, 7545–7555. [CrossRef]
22. Su, B.; Wang, B.; Luo, L.; Wang, L.; Li, B.; Liu, C.; Su, Y.; Xu, Y.; Huang, H.; Guo, J.; et al. Tuning microstructure and enhancing corrosion property of Ti-6Al-3Nb-2Zr-1Mo alloy through electron beam surface melting. *Corros. Sci.* **2022**, *206*, 110520. [CrossRef]
23. Madapana, D.; Bathe, R.; Manna, I.; Majumdar, J. Studies on Surface Characteristics and Biocorrosion Behavior of Ultrafast Laser-Structured Titanium Alloy (Ti6Al4V). *Phys. Status Solidi A* **2024**, *221*, 2300610. [CrossRef]

24. Sharma, A.; Oh, M.; Kim, J.; Srivastava, A.; Ahn, B. Investigation of electrochemical corrosion behavior of additive manufactured Ti-6Al-4V alloy for medical implants in different electrolytes. *J. Alloys Compd.* **2020**, *830*, 154620. [CrossRef]
25. Liao, S.; Zhang, S.; Song, Z.; Yang, L.; Yang, C.; Zheng, J.; Zhou, Z. Effect of Annealing on Mechanical and Biological Properties of Titanium Alloy Tantalum Coating. *Surf. Technol.* **2024**, *53*, 184–192.

Disclaimer/Publisher's Note: The statements, opinions and data contained in all publications are solely those of the individual author(s) and contributor(s) and not of MDPI and/or the editor(s). MDPI and/or the editor(s) disclaim responsibility for any injury to people or property resulting from any ideas, methods, instructions or products referred to in the content.